sciendo
Power Electronics and Drives
Volume 10(45), 2025 DOI: 10.2478/pead-2025-0005

Computationally Efficient Model Predictive Control of Delta-Connected CHB-Based Active Power Filter

Research paper

Zdeněk Kehl*, Tomas Glasberger, Zdeněk Peroutka

University of West Bohemia, RICE, Pilsen, Czech Republic

Received: 03 January, 2025; Accepted: 20 January, 2025

Abstract: This paper introduces a novel control strategy for shunt-type active power filters (APF) using a cascaded H-bridge (CHB) topology in a delta connection. The control is tailored particularly for low-cost microcontrollers with limited computation power and resources. The control combines the modified instantaneous active-reactive power (PQ) theory for power grid control and subordinated optimized (two-step) finite control set model predictive control (FCS-MPC) for control of CHB converters. The power grid control generates setpoints for CHB converters, i.e. grid compensation currents and current references securing active power delivery for DC-links of CHB converters of the APF. The two-step FCS-MPC controls the CHBs, generates phase grid compensation currents, and balances the DC-link capacitors of the CHBs. Extensive simulations and experiments on the developed 60 kW prototype of APF validate the proposed control. The results show that the control quality is comparable to the full-state FCS-MPC, while its computation time and complexity are notably reduced.

Keywords: *active power filter • grid tied converters • FCS-MPC • CHB converter • power grid quality*

1. Introduction

US$ 6.7 billion per year (Milanović, 2013) is the estimated cost loss in industrial production due to disturbances in power grids. Customers are strictly charged with power quality standards violations by electricity distributors, with an estimated penalty optimum of around 8% of electricity costs (Tadayon et al., 2021). These facts highlight how new technology taking care of power quality is essential. Power grids often accommodate inductive, non-linear, and non-symmetrical loads, which are the conventional sources of power quality problems such as reactive power consumption, higher-harmonic load currents and resulting grid voltage harmonics, and power-grid non-symmetries. Moreover, with the fast growth of renewable energy sources in recent years, such as solar and wind, maintaining the power quality and stability of power grids has become even more challenging (Liang, 2016). The massive penetration of power electronics technology, which is dominating in low-voltage grids and rapidly advancing into medium- and high-voltage power grids, brings new phenomena from the power quality point of view. Power quality, specifically reactive power and grid harmonics compensation, which is the main topic of this paper, can generally be solved by passive, active, or hybrid solutions. Passive filters are characterized by simplicity and cost-effectiveness but may encounter issues such as resonance and fixed compensation (Chauhan and Thakur, 2016). Active power filters (APFs) demonstrate superior efficacy in compensating for grid harmonics. They can dynamically adapt to changing grid conditions and improve performance compared with passive filters (Babu et al., 2021; Sanjan et al., 2020; Satpathy and De, 2024). Hybrid filters offer advantages of both previous types. However, hybrid filters often require many passive components and transformers, which can increase the complexity and dimensions of the

* *Email: kehlz@fel.zcu.cz*

system. This can render the design and maintenance more challenging than active filters, which typically comprise fewer components. The combination of passive components in hybrid filters may also cause resonance problems. This can affect the filtering characteristics and potentially induce system instability (Limongi et al., 2015; Su et al., 1998). Thus, APFs are the most prospective technology for addressing power quality issues, particularly in the case of the dynamic compensation of harmonics and reactive power (Sanjan et al., 2020; Wodyk and Iwanski, 2024).

There are several conventional configurations of APFs. Serial APFs are primarily used to address voltage distortion issues in electrical systems. These devices are designed to transform distorted grid voltage into harmonic voltage. Serial APFs can also serve as line conditioners regulating the supply voltage at the ends of a power distribution grid to meet relevant standards (Hrbac et al., 2017). The shunt APFs are connected in parallel with the load and are commonly used to compensate for current harmonics (Tareen and Mekhielf, 2018; Ullah and Ashraf, 2019). While two-level voltage-source inverters are commonly used in low-voltage grids, multilevel configurations have become increasingly popular for medium-voltage applications (Abu-Rub et al., 2010; Leon et al., 2017). Cascaded H-bridge (CHB) and multilevel modular converter (M2C) topologies are the most promising for APFs in medium- and high-voltage applications. The CHB topology offers several advantages over other multilevel configurations. This technology offers high modularity and scalability, interesting voltage-balancing capabilities, separated DC sources, harmonic reduction, reliability, and reduced stress on switching devices (Gadalla et al., 2017; Pereda and Dixon, 2012).

The conventional control of APFs is implemented through cascaded proportional-integral (PI) or proportional-resonant (PR) based control systems. Nowadays, PR controllers offering enhanced reference-tracking performance and selective harmonic compensation are the mainstream (Teodorescu et al., 2006). Some modifications in the basic control approaches must be adopted to address special operating conditions with partial improvements under specific circumstances, such as operation under unbalanced grid conditions (Behrouzian, 2017). Recently published model predictive-based controls (MPC) of APFs beat conventional PI- or PR-based control systems. Finite control set MPC (FCS-MPC) has gained attention for its straightforward application in power electronics converters, which naturally have a finite set of power circuit switching combinations. Moreover, this control can easily incorporate constraints and provide fast transient responses (Ferreira et al., 2018). For instance, in grid-connected inverters with LCL filters, cascaded MPC has demonstrated improved resonance damping and dynamic performance compared with conventional PI control methods (Zhou and Preindl, 2022). MPC has some drawbacks (e.g. computational demands and weighting factor problems) that can be solved by combining the above-mentioned approaches (Benhamadouche et al., 2023). An appropriate combination of PI and MPC approaches can mitigate model mismatches and improve the dynamic response (Morales-Caporal et al., 2024; Po et al., 2018). Other approaches can be found in the literature to decrease the computational demands of MPC methods based on the selection and reduction of the number of switching combinations (He et al., 2023) or dual-layer control approaches (Xiao et al., 2023).

Concerning the aforementioned state of the art, this paper focuses on multilevel shunt-type APFs and their control using the recent MPC theory. Specifically, the paper reports on APF based on CHB topology in a delta connection with four H-bridge converters in one branch of the delta connection, which introduces a nine-level output voltage configuration. This converter has an eligible total harmonic distortion (THD) of the controlled current without a bulky filter. However, its conventional full-state FCS-MPC control is a significant computational burden (Karamanakos et al., 2014). Therefore, we proposed a computationally lighter control employing a new two-step FCS-MPC technique specifically designed for ‘low-cost’ microcontrollers with limited computation power and resources. The proposed control is able to generate the required higher-order current harmonics as well as reactive power. Thus, it can serve as a conventional APF (higher-order harmonics compensator) and/or as the STATCOM. The control integrates a modified instantaneous active-reactive power (PQ) theory for immediate grid analysis (Akagi et al., 2007) and the calculation of phase current references with a subordinated two-step finite control set model predictive control (FCS-MPC) securing demanded currents generation and balancing of the DC-link voltages of CHB converters. The paper proves, by extensive simulations and experiments performed on the developed 60 kW prototype of shunt APF, that the proposed two-step MPC solution achieves comparable results with a full-state FCS-MPC with significantly reduced computation times. Another advantage of the proposed control is that the weighting factor, usually used for multicriteria MPC, is neglected. In this paper, the proposed control (Section 3) is supported by the introduction of a power circuit configuration of the investigated APF and designed testbed (Section 2), deriving detailed mathematical models (Section 3), extensive simulation results (Section 4), and experiments (Section 5).

2. Power Circuit Configuration of Investigated APF

The topology of the proposed APF is illustrated in Figure 1. The three-phase APF is connected to the line-to-line voltages of the power grid. A transformer is positioned between the APF and the power grid to ensure galvanic separation and voltage level adaptation of the APF. Resistance R_T and inductance L_T represent the transformer (its total resistance and total leakage inductance). The three-phase APF can be split into three single-phase APFs configured in a delta connection. Single-phase APF contains a multilevel CHB-based converter. The multilevel converter comprises the 9L-CHB topology (four H-bridge cells in series, designated Cell-A, …, Cell-D in Figure 1). The delta connection of those three 9L-CHB converters represents the power electronics part of the APF. All cells are powered by the energy drawn from the power grid; therefore, there are no additional power sources for charging the individual DC links of H-bridge converters. Each branch of the delta connection is equipped with inner identical inductance L_1, L_2, and L_3. These inductances limit the current peaks during the switching of the power converters. The three-phase power grid comprises three voltage sources u_U, u_V, and u_W, which generate three-phase grid voltages with predetermined phase shifts.

The main goal of the proposed APF's control is to compensate for the distorted load current to push the grid currents i_U, i_V, and i_W to be as close as possible to a sinewave. A three-phase diode bridge rectifier was employed as

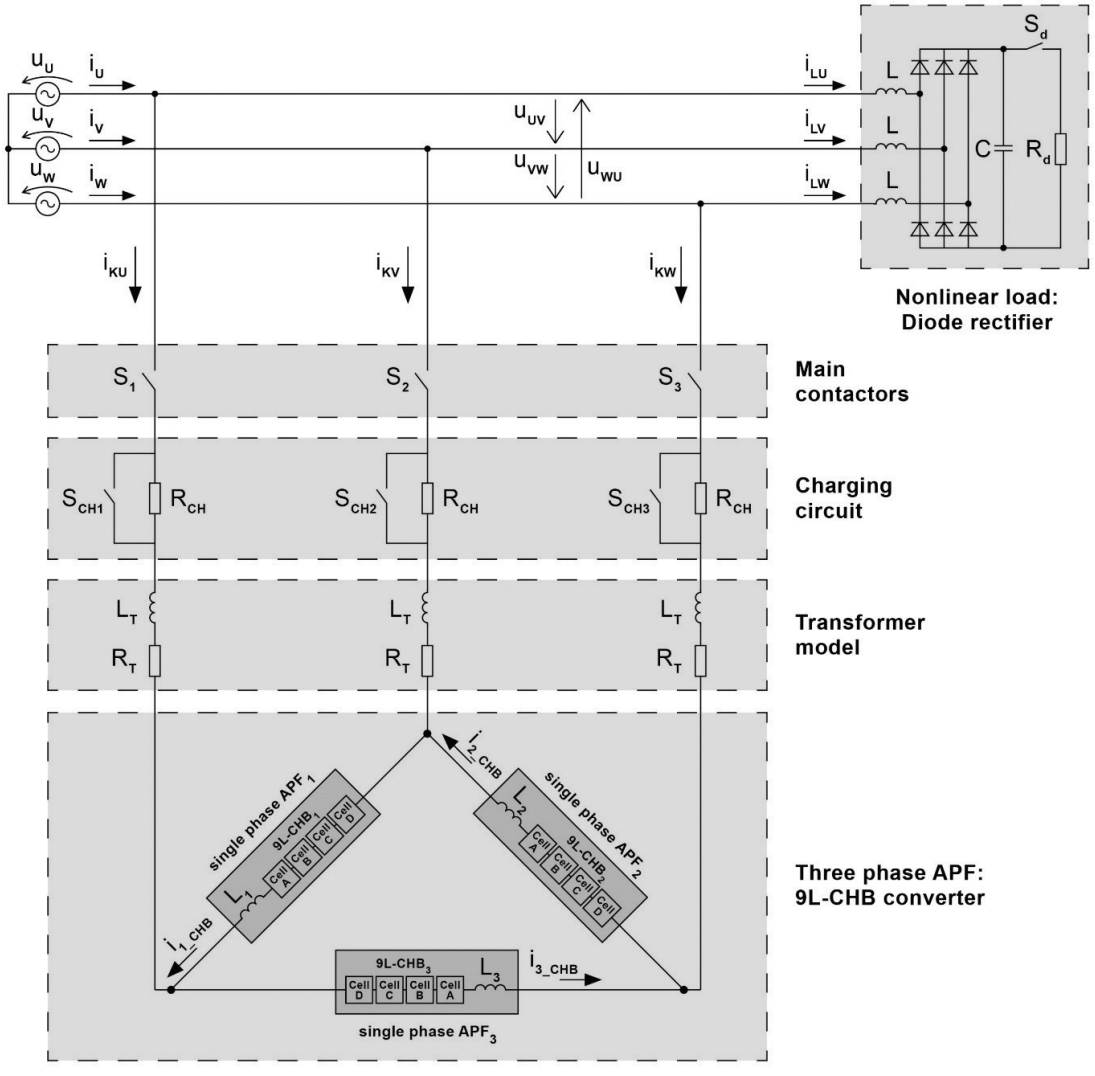

Figure 1. Power circuit configuration of investigated APF and designed testbed. APF, active power filters; CHB, cascaded H-bridge.

the grid load to simulate higher harmonics distortion in the load currents i_{LU}, i_{LV}, and i_{LW}. The diode rectifier, having the capacitor bank at its DC terminals where the resistive load is also connected, draws a highly distorted current with significant harmonic content from the power grid. In addition, three equal inductances L are inserted between the power grid and the diode rectifier, one for each phase. It causes the current taken from the power grid to be phase-shifted relative to the grid voltage. This setup is used to test whether the proposed system can effectively compensate for such distorted currents, demonstrating the overall performance of the proposed control system. The load value can be altered during operation using switch S_d to emulate the load transients in the power grid.

3. Proposed Control of the APF

The proposed APF control strategy addresses two key targets: (i) mitigation of power grid harmonics and (ii) reactive power compensation of the grid (STATCOM function). The proposed control (Figure 2) is split into two main tasks that can be interpreted as the two levels of APF's control: (1) power grid control and subordinate (2) control of CHB converters forming the APF hardware. Moreover, the three-phase APF is split into three independent single-phase APFs; therefore, the control optimization task is executed independently for each phase of APF (exactly, independently for each branch = CHB converter). The assumption of independent control of each APF's branch is essential for the theory below.

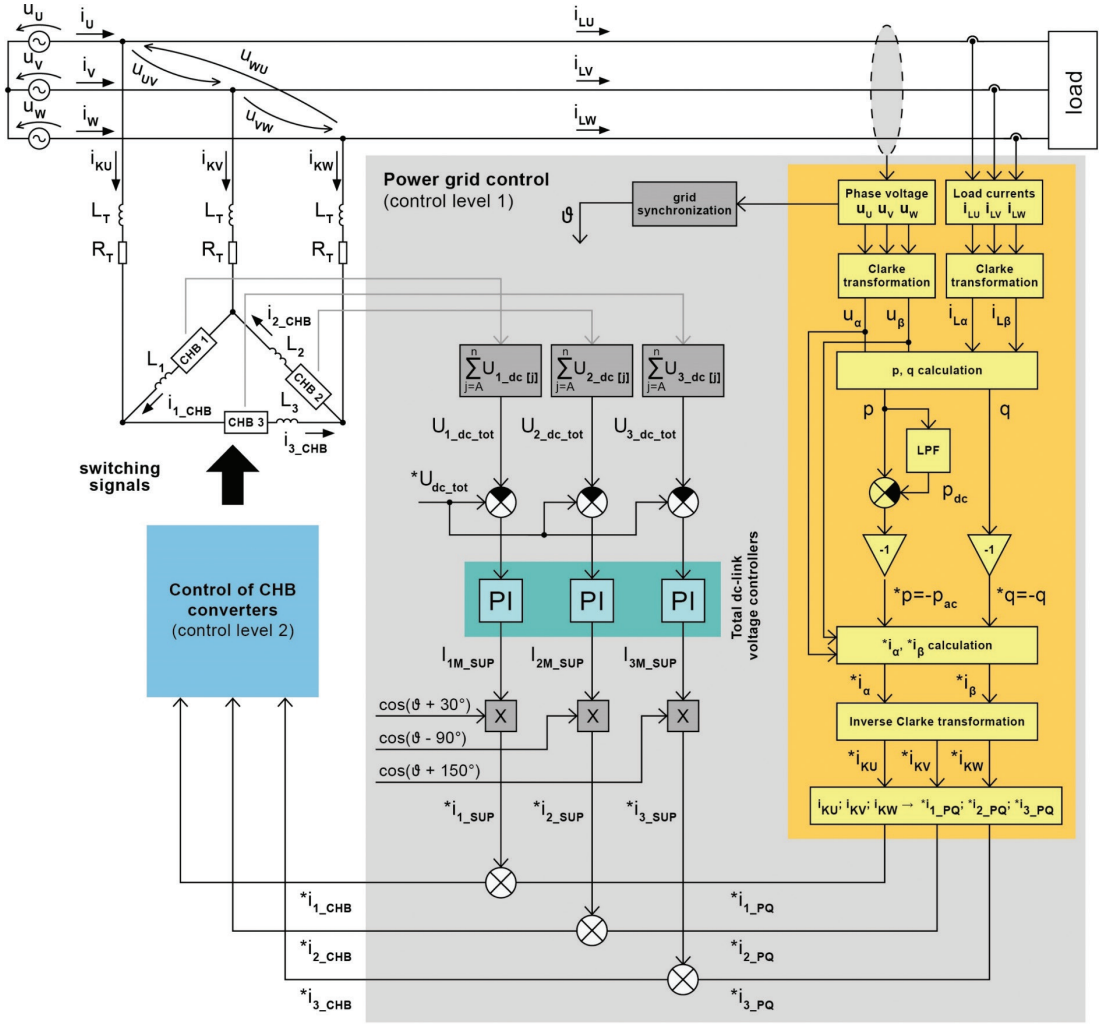

Figure 2. Proposed two-level control of shunt APF based on CHB converters in delta connection. APF, active power filter; CHB, cascaded H-bridge; LPF, low pass filtration.

The power grid control uses modified instantaneous active-reactive power (PQ) theory for immediate grid analysis (Akagi et al., 2007) and generation of setpoints/references for CHB converters. It is responsible for generating grid compensation current comprising higher-harmonics current references for grid harmonics mitigation and generation of current references for reactive power compensation. The last significant role of power grid control is the generation of current references to secure power supply (i.e. active power delivery) for DC-links of CHB converters of the APF.

The control of CHB converters uses the new two-step FCS-MPC strategy. The input to this control is the CHB converter current reference generated by the power grid control as described above. The control of the CHB converter is divided into two steps, but both steps use the FCS-MPC background. Step 1 is responsible for the CHB converter current control. However, the optimization process (precisely, model calculation) is not executed for all available switching combinations. The CHB converter switching combinations are offline sorted into groups based on the voltage at the CHB converter AC terminals. Thus, the output of step 1, which is the input to step 2, is the selected group of switching combinations. Step 2 is responsible for balancing DC-link voltages in CHB converter cells. Exactly, step 2 chooses the switching combination from the preselected group, leading to the best solution from the DC-link voltages of CHB converter cells from a balancing viewpoint. The FCS-MPC is solved on the horizon length of 1.

3.1. Power grid control

Power grid control (=control level 1) generates the reference currents for the CHB converter current control (=control level 2). The demanded CHB converter current (in case of 3ph APF—the problem is solved as a control of three independent single-phase APFs—the currents are denoted $^{*}i_{1\_CHB}$, $^{*}i_{2\_CHB}$, $^{*}i_{3\_CHB}$) is the sum of the grid compensation current (denoted $^{*}i_{1\_PQ}$, $^{*}i_{2\_PQ}$, $^{*}i_{3\_PQ}$) and power supply current securing charging of DC-links of CHB converter cells (denoted $^{*}i_{1\_SUP}$, $^{*}i_{2\_SUP}$, $^{*}i_{3\_SUP}$):

$$ {}^{*}\boldsymbol{i}_{\boldsymbol{CHB}} = \begin{bmatrix} {}^{*}i_{1\_CHB} \\ {}^{*}i_{2\_CHB} \\ {}^{*}i_{3\_CHB} \end{bmatrix} = \begin{bmatrix} {}^{*}i_{1\_PQ} \\ {}^{*}i_{2\_PQ} \\ {}^{*}i_{3\_PQ} \end{bmatrix} + \begin{bmatrix} {}^{*}i_{1\_SUP} \\ {}^{*}i_{2\_SUP} \\ {}^{*}i_{3\_SUP} \end{bmatrix} \tag{1} $$

3.1.1. Grid compensation current reference

The PQ theory analyses the instantaneous state of the power grid. Measured instantaneous values of grid voltages and load currents are used after Clarke's transformation Eqs (2) and (3) to calculate the instantaneous active and reactive powers in the power grid Eq. (4). The zero-sequence component can be neglected as the three-phase power grid without a ground line is considered. The calculated active and reactive powers are input signals for determining the grid compensation current.

$$ \boldsymbol{i}_{\boldsymbol{L}} = \begin{bmatrix} i_{L\alpha} \\ i_{L\beta} \end{bmatrix} = \sqrt{\frac{2}{3}} \cdot \begin{bmatrix} 1 & -\frac{1}{2} & -\frac{1}{2} \\ 0 & \frac{\sqrt{3}}{2} & -\frac{\sqrt{3}}{2} \end{bmatrix} \cdot \begin{bmatrix} i_{LU} \\ i_{LV} \\ i_{LW} \end{bmatrix}, \tag{2} $$

$$ \boldsymbol{u} = \begin{bmatrix} u_{\alpha} \\ u_{\beta} \end{bmatrix} = \sqrt{\frac{2}{3}} \cdot \begin{bmatrix} 1 & -\frac{1}{2} & -\frac{1}{2} \\ 0 & \frac{\sqrt{3}}{2} & -\frac{\sqrt{3}}{2} \end{bmatrix} \cdot \begin{bmatrix} u_{U} \\ u_{V} \\ u_{W} \end{bmatrix}. \tag{3} $$

The complex instantaneous power $\boldsymbol{s}$ is given by the product of the grid voltage vector $\boldsymbol{u}$ and conjugate load current vector $\boldsymbol{i}_{\boldsymbol{L}}^{*}$:

$$ s = \boldsymbol{u}.\boldsymbol{i}_{\boldsymbol{L}}^{*} = \left(u_{\alpha} + ju_{\beta}\right) \cdot \left(i_{L\alpha} - ji_{L\beta}\right). \tag{4} $$

The active and reactive powers are calculated as the real and imaginary parts of the complex power, respectively:

$$s = \begin{bmatrix} p \\ q \end{bmatrix} = \begin{bmatrix} u_\alpha & u_\beta \\ -u_\beta & u_\alpha \end{bmatrix} \cdot \begin{bmatrix} i_{L\alpha} \\ i_{L\beta} \end{bmatrix}. \tag{5}$$

The instantaneous reactive power q defines the energy that degrades the overall quality of the electrical energy. The required reactive power $^*q$ must be negative compared to the calculated reactive power because the APF should compensate for this value:

$$^*q = -q. \tag{6}$$

The demanded active power $^*p$ is derived from Eq. (5) by subtracting the DC component of the active power p_{dc}, which is obtained by low pass filtration (LPF) from calculated active power p. The cutoff frequency of the LPF was set to 16 Hz.

$$^*p = -\left(p - p_{dc}\right) = -p_{ac}. \tag{7}$$

When the required active and reactive powers are defined, the reverse calculation follows. In the first step, the required $\alpha\beta$ currents are calculated as

$$\begin{bmatrix} ^*i_\alpha \\ ^*i_\beta \end{bmatrix} = \frac{1}{u_\alpha^2 + u_\beta^2} \cdot \begin{bmatrix} u_\alpha & u_\beta \\ u_\beta & -u_\alpha \end{bmatrix} \cdot \begin{bmatrix} ^*p \\ ^*q \end{bmatrix}, \tag{8}$$

and phase grid compensation currents

$$\begin{bmatrix} ^*i_{KU} \\ ^*i_{KV} \\ ^*i_{KW} \end{bmatrix} = \sqrt{\frac{2}{3}} \cdot \begin{bmatrix} 1 & 0 \\ -\frac{1}{2} & \frac{\sqrt{3}}{2} \\ -\frac{1}{2} & -\frac{\sqrt{3}}{2} \end{bmatrix} \cdot \begin{bmatrix} ^*i_\alpha \\ ^*i_\beta \end{bmatrix}. \tag{9}$$

The next step is the recalculation of phase grid compensation currents $^*i_{KU}$, $^*i_{KV}$, $^*i_{KW}$ to the demanded currents of particular CHB converters of APF in delta connection:

$$\begin{bmatrix} ^*i_{1\_PQ} \\ ^*i_{2\_PQ} \\ ^*i_{3\_PQ} \end{bmatrix} = \frac{1}{3} \cdot \begin{bmatrix} ^*i_{KV} - {}^*i_{KU} \\ ^*i_{KW} - {}^*i_{KV} \\ ^*i_{KU} - {}^*i_{KW} \end{bmatrix}. \tag{10}$$

3.1.2. Current reference for active power delivery to DC-links of CHB converter

The demanded overall active power is defined in Akagi et al. (2007). However, the primary limitation of this approach is that there can be differences among DC-links in each CHB converter, and the algorithm cannot identify them and ensure their energy balancing. This problem is solved by three PI controllers responsible for independent active power reservation for each CHB converter. Each PI controller (called 'total DC-link voltage controller') controls the total DC-link voltage of the corresponding CHB converter. Thus, the setpoint voltage for these controllers is given by the number of cells (m) multiplied by the reference DC-link voltage of one cell (U_{dc_ref}):

$$^*U_{dc\_tot} = m \cdot U_{dc\_ref} \tag{11}$$

The total DC-link voltage controller's feedback is the sum of the DC-link voltages of all cells of individual CHB converters. The outputs of these controllers (denoted I_{1M_SUP}, I_{2M_SUP}, I_{3M_SUP}) set the amplitudes of demanded DC-link power supply currents ($^{*}i_{1\_SUP}$, $^{*}i_{2\_SUP}$, $^{*}i_{3\_SUP}$). The power supply current corresponds to the active power needed to achieve the appropriate sum of DC-link voltages of the cells of the given CHB converter. Thus, the power supply current is in phase with the line-to-line voltage corresponding to the given CHB converter. The phase of the power supply current is calculated from the grid voltage vector position (ϑ) in the stationary reference frame (α, β). The block 'grid synchronization' provides the grid voltage vector position. The position (ϑ) can be extracted directly from Eq. (3) in simple cases, or more advanced SOGI-PLL (e.g. Blahnik et al., 2018) is recommended to find ϑ reliably. The power supply currents for individual CHB converters of the APF are given by Eqs (12)–(14):

$$^{*}i_{1\_SUP} = I_{1M\_SUP} \cdot cos(\vartheta + 30°) \tag{12}$$

$$^{*}i_{2\_SUP} = I_{2M\_SUP} \cdot cos(\vartheta - 90°) \tag{13}$$

$$^{*}i_{3\_SUP} = I_{3M\_SUP} \cdot cos(\vartheta + 150°) \tag{14}$$

3.2. Two-step FCS-MPC of CHB converters

As described above, the control of the investigated 3-ph APF has been decomposed into the control of three independent single-phase APFs, each configured as the CHB converter. The control theory presented in this paper is formulated for a general *n*-level CHB converter. The proposed two-step FCS-MPC has two main responsibilities: (i) generation of specific waveforms of compensation current (fundamental + higher harmonics), which is the output of superior power grid control described in Section 3.1, and (ii) proper balancing of DC-link voltages in the CHB converter cells. Step 1 secures the control target (i), and step 2 solves the control target (ii). The FCS-MPC is solved in both steps on the horizon length of 1.

The success of FCS-MPC strongly depends on the quality of the mathematical model. Similarly to the control, the proposed model is divided into two parts with different scales. The first model (Figure 3) used in step 1 describes

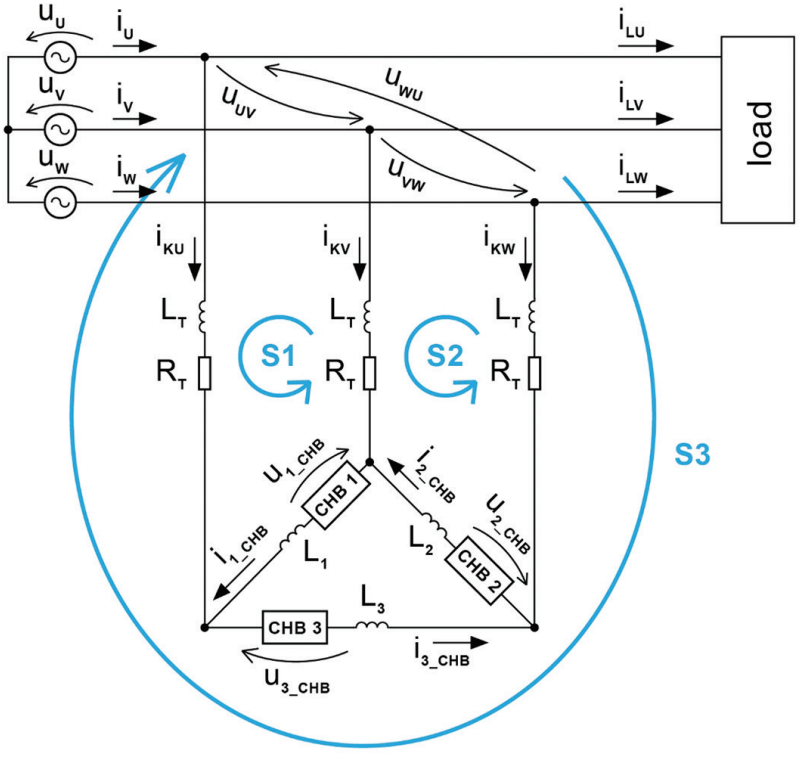

Figure 3. Model for step 1 of FCS-MPC: Power circuit configuration used for the derivation of the mathematical model describing the interaction between the power grid and CHB converter. CHB, cascaded H-bridge; FCS-MPC, finite control set model predictive control.

the relationship/interaction between the power grid and the given CHB converter, which is, in this model, replaced by the equivalent voltage source. The second part used in step 2 describes the behaviour of the CHB power circuit—precisely, the behaviour of DC-links of CHB converter cells. Thus, the first model is superior to the second.

3.2.1. Step 1 of FCS-MPC—CHB converter current control

The input to this control is the demanded CHB converter current, which is the corresponding term of the following vector $^{*}i_{CHB} = [^{*}i_{1\_CHB,}\ ^{*}i_{2\_CHB,}\ ^{*}i_{3\_CHB}]^{T}$ generated by power grid control (Section 3.1). To reduce computational time and complexity, the control optimization process (specifically, model calculation) is not executed for all available switching combinations. The CHB converter switching combinations are offline sorted into groups based on the voltage at the CHB converter AC terminals. The group members are switching combinations that create the same voltage. In the case of a single-phase CHB converter, the sorting of the switching combinations is trivial. The number of groups is the same as the number of CHB converter levels. Thus, for example, for the nine-level CHB converter (this is the configuration of the built prototype), the optimization (model calculation) is executed nine times. The voltage at the 9L-CHB converter AC terminals u_{l_CHB} in the *l*-phase of APF (*l* = 1, 2, 3) can achieve the following nine discrete values:

$$u_{l\_CHB} \in \left\{ U_{l\_dc\_tot}, \frac{3}{4}U_{l\_dc\_tot}, \frac{1}{2}U_{l\_dc\_tot}, \frac{1}{4}U_{l\_dc\_tot}, 0, -\frac{1}{4}U_{l\_dc\_tot}, -\frac{1}{2}U_{l\_dc\_tot}, -\frac{3}{4}U_{l\_dc\_tot}, -U_{l\_dc\_tot} \right\}, \quad (15)$$

where $U_{l\_dc\_tot}$ is the sum of measured DC-link voltages in all CHB converter cells in the *l*-phase of APF (*l* = 1, 2, 3). The symmetry of considered voltage levels requires a successful balancing of the DC-links of all CHB converter cells. The mathematical model used in this step is presented in Figure 3. It consists of a three-phase power grid, which is represented by three voltage sources u_U, u_V, and u_W. The grid voltages $\boldsymbol{u}$ are measured. The CHB converter is connected to the terminals of the line-to-line voltages. The given CHB converter is replaced in the model by an equivalent voltage source (u_{1_CHB}, u_{2_CHB}, u_{3_CHB}) with a finite set of achievable voltages according to Eq. (15). The transformer placed between APF and the power grid is represented by its short-circuit impedance L_T and R_T. The load is assumed to be three-phase and non-linear. The load is in the model replaced by current sources—their values are the measured currents $\boldsymbol{i}_L$ Eq. (2).

The model is described in Eq. (16), which is derived by application of the second Kirchhoff's law in the vector form:

$$\boldsymbol{u}_S = R_T \cdot \boldsymbol{i}_K + L_T \frac{d\boldsymbol{i}_K}{dt} - L_{IN} \frac{d\boldsymbol{i}_{CHB}}{dt} + \boldsymbol{u}_{CHB} - R_T \cdot \boldsymbol{i}'_K - L_T \frac{d\boldsymbol{i}'_K}{dt} \quad (16)$$

The vector $\boldsymbol{u}_S = [u_{UV}, u_{VW}, u_{WU}]^T$ represents power grid line-to-line voltages. The phase grid compensation currents are defined by vector $\boldsymbol{i}_K = [i_{KU}, i_{KV}, i_{KW}]^T$. All CHB converter inductances are assumed to be equal ($L_1 = L_2 = L_3$); therefore, they can be substituted by the common parameter L_{IN}. The vector of CHB converters currents is $\boldsymbol{i}_{CHB} = [i_{1\_CHB}, i_{2\_CHB}, i_{3\_CHB}]^T$. The output voltages of all CHB converters are defined by vector $\boldsymbol{u}_{CHB} = [u_{1\_CHB}, u_{2\_CHB}, u_{3\_CHB}]^T$. The vector $\boldsymbol{i'}_K$ represents phase grid compensation currents as vector $\boldsymbol{i}_K$, but the components are in a different order. The vector $\boldsymbol{i'}_K$ is defined $\boldsymbol{i'}_K = [i_{KV}, i_{KW}, i_{KU}]^T$. The model considers the following configuration:

$$\begin{bmatrix} i_{KU} \\ i_{KV} \\ i_{KW} \end{bmatrix} = \begin{bmatrix} i_{3\_CHB} \\ i_{1\_CHB} \\ i_{2\_CHB} \end{bmatrix} - \begin{bmatrix} i_{1\_CHB} \\ i_{2\_CHB} \\ i_{3\_CHB} \end{bmatrix} \quad (17)$$

$$i_{KU} + i_{KV} + i_{KW} = 0 \quad (18)$$

$$i_{1\_CHB} + i_{2\_CHB} + i_{3\_CHB} = 0 \quad (19)$$

Eq. (16) can be modified to the required form using the aforementioned assumptions and Kirchhoff's laws. The Euler method was employed for the discretization of derived equations. The discrete mathematical

model in vector form describing relationships between the power grid and CHB converter is defined in Eq. (20):

$$\boldsymbol{i}_{CHB[k+1]} = \left(1 - \frac{3R_T \cdot \Delta T}{L_{IN} + 3L_T}\right) \cdot \boldsymbol{i}_{CHB[k]} - \frac{\Delta T}{L_{IN} + 3L_T} \cdot \boldsymbol{u}_{S[k]} + \frac{\Delta T}{L_{IN} + 3L_T} \cdot \boldsymbol{u}_{CHB[k]}. \tag{20}$$

In this step, the output voltage of each CHB converter (each term of vector $\boldsymbol{u}_{CHB}$) consists of nine discrete states as was defined in Eq. (15). The proposed cost function for step 1 is defined in Eq. (21):

$$arg\ min\ J_{l\_I} = \left({}^{*}i_{l\_CHB} - i_{l\_CHB[k+1]}\right)^2 + I_{lim}, \tag{21}$$

where index $l = 1, 2, 3$ indicates a particular phase of APF. The current limitation (constraint) is represented by I_{lim}. This is a binary criterion that limits current i_{l_CHB} flowing through the CHB converter in the l-phase of the APF. This limitation ensures that the current will not be higher than the set limit I_{MAX}. The criterion I_{lim} is defined by:

$$I_{lim} = \begin{cases} 0, |i_{l\_CHB\ [k+1]}| < I_{MAX} \\ \lambda, |i_{l\_CHB\ [k+1]}| \geq I_{MAX} \end{cases}, \tag{22}$$

where λ represents the penalty factor. In our case, $\lambda = 10^{12}$. The control optimization is executed independently for each CHB converter. Thus, only currents corresponding to the given CHB converter take place in Eq. (21) calculation. The output of step 1 is the selection of the best voltage group.

3.2.2. Step 2 of FCS-MPC—balancing DC-links of CHB converter cells

The input to step 2 is the preselected voltage group, which is the output of step 1. The control target for step 2 is an exploration of all the members of the selected voltage group, i.e. exploration of all CHB converter switching combinations generating voltage defined for the given voltage group and selection of the best switching combination securing CHB current command as well as the best DC-link balancing of the given cells. Appendix I contains a comprehensive table of all switching combinations for the 9L-CHB (the configuration of the built prototype), systematically organized into nine groups, each corresponding to one output voltage level of the 9L-CHB. One group is selected based on the optimal voltage level found in step 1, wherein the cost function Eq. (25) proposed for step 2 is subsequently evaluated. The most computationally intensive scenario, i.e. group 4 (zero level) consisting of 19 redundant switching combinations, requires 28 calculations of the mathematical model (9 calculations in step 1 and 19 calculations in step 2). In contrast, the conventional full-state FCS-MPC consistently computes all 81 combinations for each CHB converter.

The model used for step 2 of FCS-MPC describes the behaviour of the CHB converter power circuit (generally in phase l) and, specifically, the DC-links of all cells. The model has been derived for the general n-level CHB converter configuration (Figure 4).

The CHB converter topology has all the cells connected in series. Thus, the CHB converter current i_{l_CHB} flows through all the cells. The general expression of capacitor current in DC-link of the j-th cell ($j = A, B, \ldots, n$) in phase $l = 1, 2, 3$ is given by the differential equation

$$i_{l\_C\_j} = C_{dc} \cdot \frac{dU_{l\_dc\_j}}{dt}. \tag{23}$$

The derivation of the capacitor voltage $U_{l\_dc\_j}$ for the individual cells can be done from Eq. (23). After discretization using the Euler's method and employing the switching function x_{l_j} (x_{l_j} couples $i_{l\_C\_j}$ and i_{l_CHB}.), the DC-link voltages in discrete form can be described by

$$\boldsymbol{U}_{l\_dc\_j[k+1]} = \boldsymbol{U}_{l\_dc\_j[k]} - \boldsymbol{x}_{l\_j} \circ \boldsymbol{i}_{CHB[k]} \frac{\Delta T}{C_{dc}}\ , \tag{24}$$

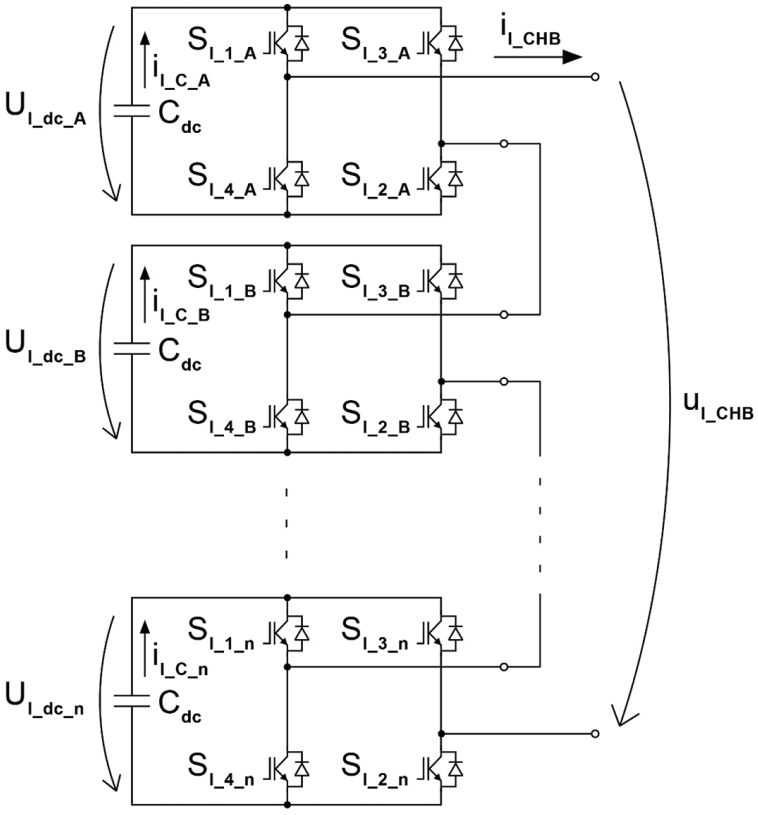

Figure 4. Model for step 2 of FCS-MPC: Power circuit used for derivation of the mathematical model describing the behaviour of a general *n*-level CHB converter. CHB, cascaded H-bridge; FCS-MPC, finite control set model predictive control.

where $\boldsymbol{U}_{l\_dc\_j} = [U_{l\_dc\_A}, U_{l\_dc\_B}, \ldots U_{l\_dc\_n}]^T$ is the vector of DC-link voltages of all CHB converter cells in phase *l*. $\boldsymbol{x}_{l\_j} = [x_{l\_A}, x_{l\_B}, \ldots x_{l\_n}]^T$ represents the vector of the switching functions; each switching function has three possible states of −1, 0, and 1 for each H-bridge cell. Relation between the switching combination of H-bridge cell and x_{l_j} is defined as $x_{l\_j} = 1$ for $S_{l\_1\_j}$, $S_{l\_2\_j}$ ($u_{l\_CHB\_j} = U_{l\_dc\_j}$); $x_{l\_j} = 0$ for $S_{l\_1\_j}$, $S_{l\_3\_j}$ or $S_{l\_2\_j}$, $S_{l\_4\_j}$ ($u_{l\_CHB\_j} = 0$); $x_{l\_j} = -1$ for $S_{l\_3\_j}$, $S_{l\_4\_j}$ ($u_{l\_CHB\_j} = -U_{l\_dc\_j}$). It corresponds with marking and orientations in Figure 4. The cost function for control and balancing of DC-link capacitors voltages of H-bridge cells, the general form for *n* cascaded converters, is given by Eq. (25):

$$arg\ min\ J_{l\_U_{dc}} = (U_{dc\_ref} - U_{l\_dc\_A\ [k+1]})^2 + (U_{dc\_ref} - U_{l\_dc\_B[k+1]})^2 + \cdots + (U_{dc\_ref} - U_{l\_dc\_n[k+1]})^2, \quad (25)$$

where index *l* = *1*, 2, 3 indicates particular phase of the APF, U_{dc_ref} represents demanded voltage in DC-link of particular H-bridge cells. The output of step 2 is the 'optimal' switching combination of the given CHB converter.

4. Simulations of the Proposed Control System

A simulation model in Mathworks' Matlab/Simulink and Plexim's PLECS was developed to perform detailed simulations and get first insights and evidence of the proper function of the proposed system. The proposed control was tested under selected transient and steady-state conditions. Special attention has been paid to the start-up of the APF and dynamic changes in power grid load. The simulations systematically compare the behaviour of the proposed two-step FCS-MPC with the conventional full-state FCS-MPC. The developed testbed is described in Section 2. Three voltage sources configured in a star connection create the power grid in the simulation model. The amplitude of the power grid voltage is set to 61 V, and the rated grid frequency is 50 Hz. The non-linear load is modelled as a three-phase diode bridge rectifier connected to the power grid through 1 mH inductances. The DC

side of the diode rectifier includes a filtering capacitor with a capacity of 3.25 mF, realized by two 6.5 mF capacitors connected in series. The diode rectifier supplies a variable load, modelled as a resistor R = 32 Ω in series with a power switch. The power switch enables the connection and disconnection of the resistive load to the DC terminals of the diode rectifier, allowing for the simulation of dynamic step changes in the load on the power grid. The control algorithm operates with a sampling period of 100 μs.

The first set of simulations (Figures 5 and 6) reports the APF's behaviour during the start-up under both proposed two-step FCS-MPC and full-state FCS-MPC. At the end of the initial pre-charging procedure (time of 0.15 s), all DC-links of each CHB converter of the APF are charged to grid maximum voltages. The grid current corresponds to the load current (Figure 6). The three-phase diode bridge rectifier represents the non-linear load of the power grid. The diode bridge rectifier is loaded by the RC load, where R = 32 Ω and C = 3.25 mF. After starting the APF control (time 0.15 s), the DC-link voltage of particular CHB converter cells rises to the demanded DC-link voltage (U_{dc_ref} = 42.5 V for each H-bridge, $*U_{dc\_tot}$ = 170 V), and the grid current started to be near sinewave. The proper function of the

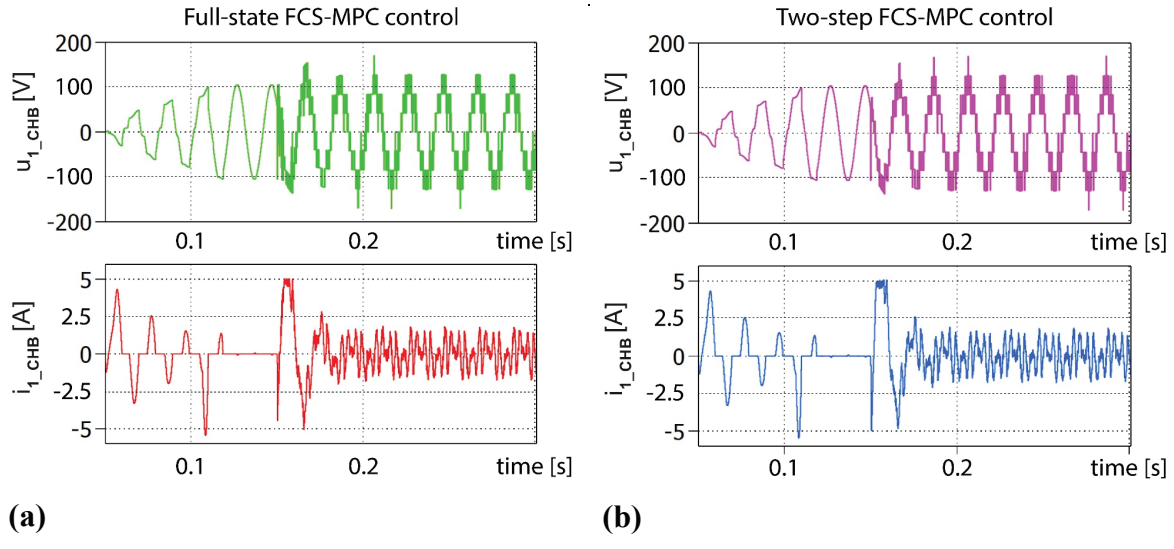

Figure 5. APF start-up: (a) full-state FCS-MPC and (b) proposed two-step FCS-MPC. The power grid is loaded by the 3ph diode rectifier supplying RC load with R = 32 Ω, C = 3.25 mF. U_{dc_ref} = 42.5 V (*U_{dc_tot} = 170 V). Green, purple: CHB converter output voltage u_{1_CHB}, red, blue: CHB converter current i_{1_CHB}. CHB, cascaded H-bridge; FCS-MPC, finite control set model predictive control; RC,

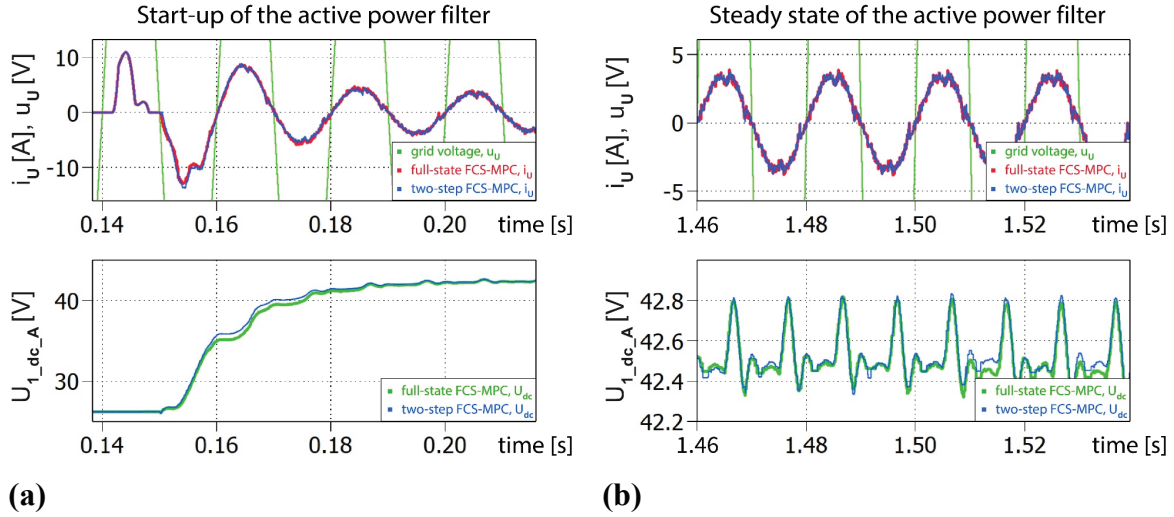

Figure 6. APF start-up analysed from the power grid viewpoint: (a) transient conditions, (b) steady-state; the same test scenario as in Figure 5. APF, active power filter.

converter current limitation can be seen in time 0.15 s. Figure 6 shows the comparison of both controls from the power grid viewpoint. Figure 6a displays the grid current i_U waveform and DC-link voltage in one CHB converter cell U1_dc_A, under the transient conditions. Figure 6b reports the identical waveforms, however, under steady-state conditions. From Figures 5 and 6, it is evident that both controls achieved similar results. Figure 7 introduces APF behaviour under step changes in grid load again under full-state FCS-MPC and two-step FCS-MPC. Figure 7a compares the dynamics during grid unloading, while Figure 7b presents the dynamics during the step increase in grid load. As in previous simulations, compensated grid currents, load currents, and DC-link capacitor voltages are displayed in one particular CHB converter.

Figures 8 and 9 report the results of a detailed analysis of compensated grid current under steady-state conditions. The distortion of the grid current can be assumed as the most important criterion for the APF. The behaviour of both control strategies exhibits strong similarities, which is further evidenced by the harmonic analysis of these waveforms presented in Figure 9. The THD of the compensated grid currents in steady state for both methods of control were calculated and are shown in Table 1. THD i_U for the full-state FCS-MPC is 9.0095% and for the two-step FCS-MPC is 9.2130%, respectively.

The impact of the variation in the key model parameters used in both evaluated controls (full-state FCS-MPC and two-step FCS-MPC) on the APF behaviour was explored. A sensitivity analysis was performed, monitoring the effect on THD of compensated grid current i_U (Figure 10). Specifically, the size of L_T and L_{IN} was gradually increased

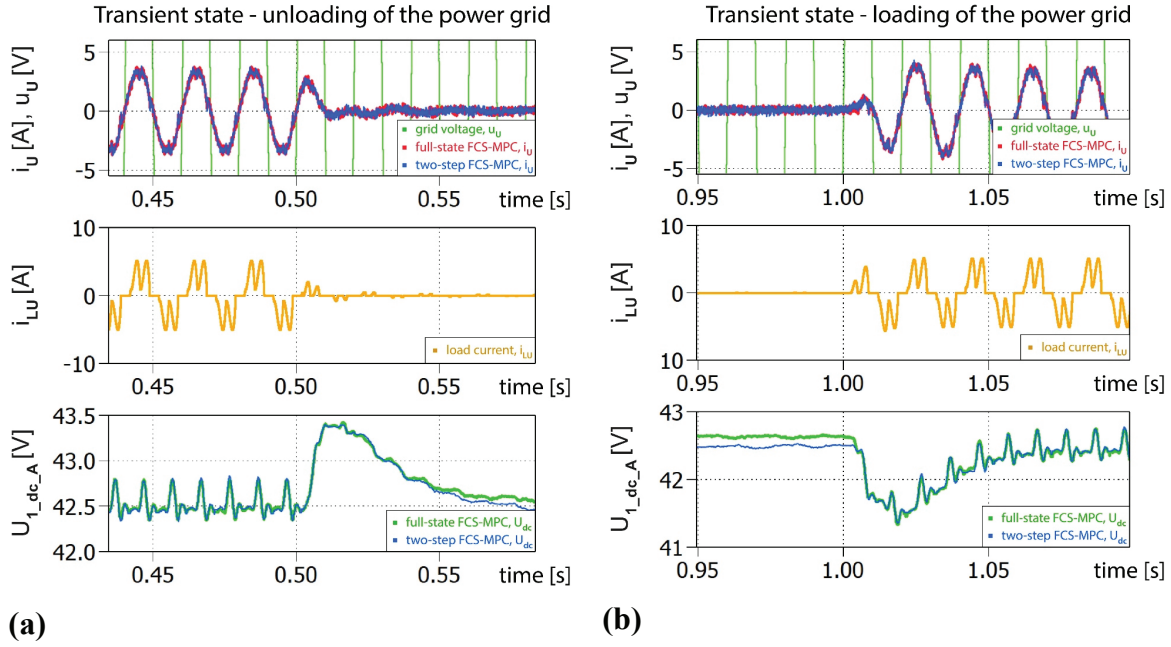

Figure 7. Comparison of full-state and two-step FCS-MPC during step unloading of the power grid in $t = 0.5$ s (a) and loading of the power grid in $t = 1$ s (b). The power grid is loaded by the 3ph diode rectifier supplying RC load with $R = 32\ \Omega$, $C = 3.25$ mF. $U_{dc\_ref} = 42.5$ V (*$U_{dc\_tot} = 170$ V). FCS-MPC, finite control set model predictive control; RC,

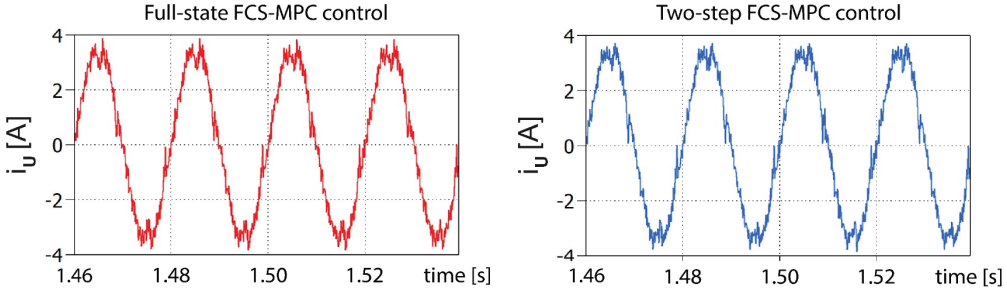

Figure 8. Detail of compensated grid currents i_U in steady-state for both the full-state FC-MPC (red) and the proposed two-step FCS-MPC (blue). FC-MPC, FCS-MPC, finite control set model predictive control.

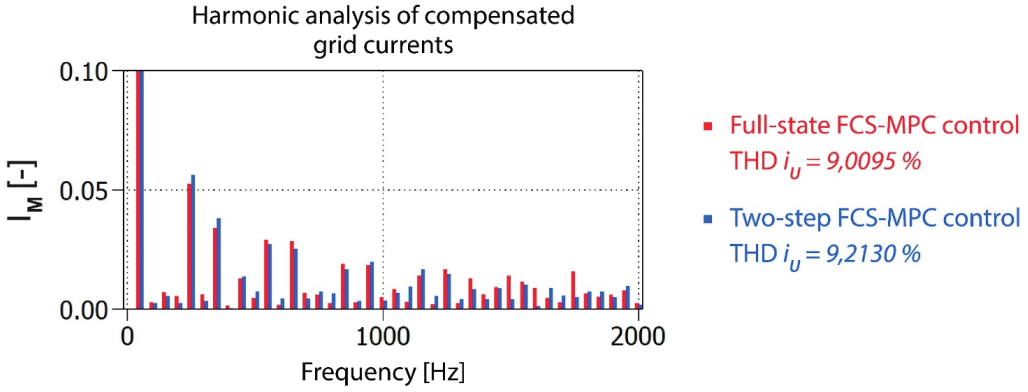

Figure 9. Harmonics analysis of compensated grid currents i_U: Red: full-state FCS-MPC, blue: two-step FCS-MPC. FCS-MPC, finite control set model predictive control; THD, total harmonic distortion.

Table 1. Harmonic analysis of currents

	Simulations		Experiments
Control strategy	Full-state FCS-MPC	Two-step FCS-MPC	Two-step FCS-MPC
THD of load current i_{LU}	54.8474%	54.8475%	41.8789%
THD of compensated grid current i_U	9.0095%	9.2130%	9.9983%

FCS-MPC, finite control set model predictive control; THD, total harmonic distortion.

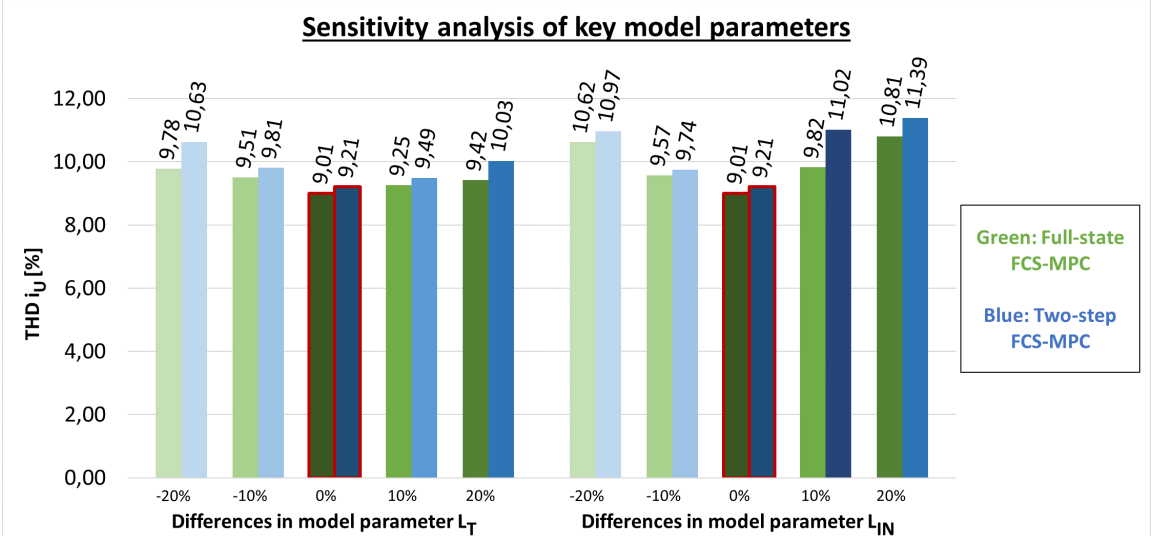

Figure 10. Sensitivity analysis of key model parameters for both mentioned control approaches (full-state FCS-MPC and two-step FCS-MPC). The power grid is symmetrical, and it is loaded by the 3ph diode rectifier supplying RC load with $R = 32\ \Omega$, $C = 3.25$ mF. FCS-MPC, finite control set model predictive control; THD, total harmonic distortion.

up to ±20%. When these parameters were changed, the THD i_U was in the worst case 10.81% for full-state FCS-MPC and 11.39% for two-step FCS-MPC. The variation of DC-link capacitors (C_{dc}) of individual CHB cells was also investigated. This did not have a significant effect on THD i_U as it is used only in the second step of the control for balancing the DC-link voltage.

Figure 11 compares both controls (full-state FCS-MPC and two-step FCS-MPC) during the start-up of APF with unbalanced initial DC-link voltages. An unbalanced initial voltage state can be caused, for example, by parameter variation in pre-charging resistances or other mismatches. In the simulation, asymmetries of +15 V and −7 V were chosen to clearly illustrate the balancing capability of the control (thus, the initial DC-link voltages in investigated

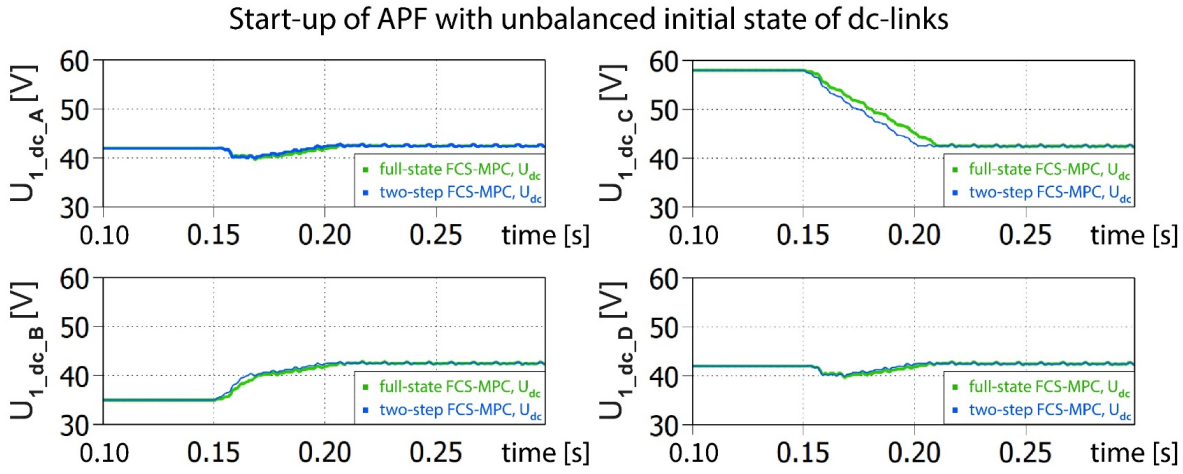

Figure 11. Comparison of full-state FCS-MPC and two-step FCS-MPC during start-up of APF with unbalanced initial DC-link voltages in one CHB converter (initial states: $U_{1\_dc\_A}$ = 42 V, $U_{1\_dc\_B}$ = 35 V, $U_{1\_dc\_C}$ = 58 V and $U_{1\_dc\_D}$ = 42 V). APF, active power filter; CHB, cascaded H-bridge; FCS-MPC, finite control set model predictive control.

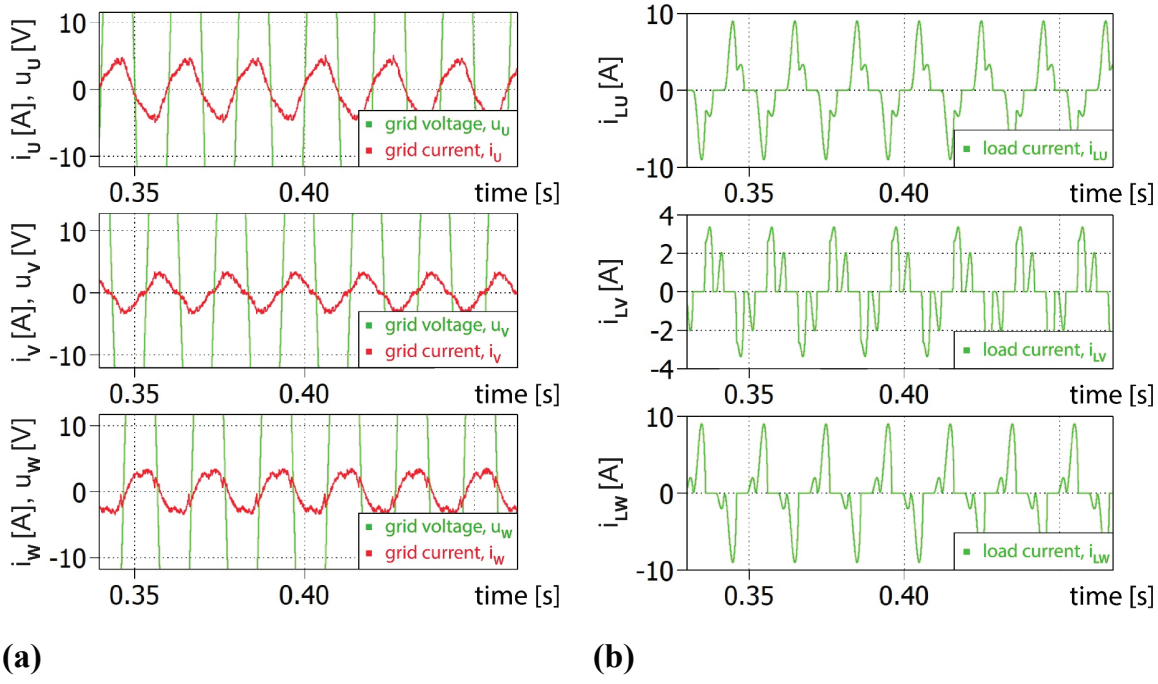

Figure 12. APF with two-step FCS-MPC control under the unbalanced power grid operation: (a) grid voltages and compensated grid currents and (b) load currents. Voltage drop in phase *V* of 10%. The power grid is loaded by the 3ph diode rectifier supplying RC load with R = 32 Ω, C = 3.25 mF. APF, active power filter; FCS-MPC, finite control set model predictive control; RC,

CHB converter cells were: $U_{1\_dc\_A}$ = 42 V, $U_{1\_dc\_B}$ = 35 V, $U_{1\_dc\_C}$ = 58 V and $U_{1\_dc\_D}$ = 42 V). The control algorithm started in time 0.15 s. It is evident that the control reliably balanced all DC-link voltages in a short time.

The operation of the investigated APF under unbalanced grid conditions is demonstrated in Figure 12, where a 10% voltage drop in phase *V* is considered. The proposed two-step FCS-MPC achieved the following THD of compensated grid currents: THD i_U = 12.85%, THD i_V = 17.48%, and THD i_W = 16.35% in comparison with THD of uncompensated load currents THD i_{LU} = 56.17%, THD i_{LV} = 86.68%, and THD i_{LW} = 79.80%. Further improvement can be ensured by modifications of the mathematical model and control to respect grid distortion (e.g. Al-Gahtani et al., 2022).

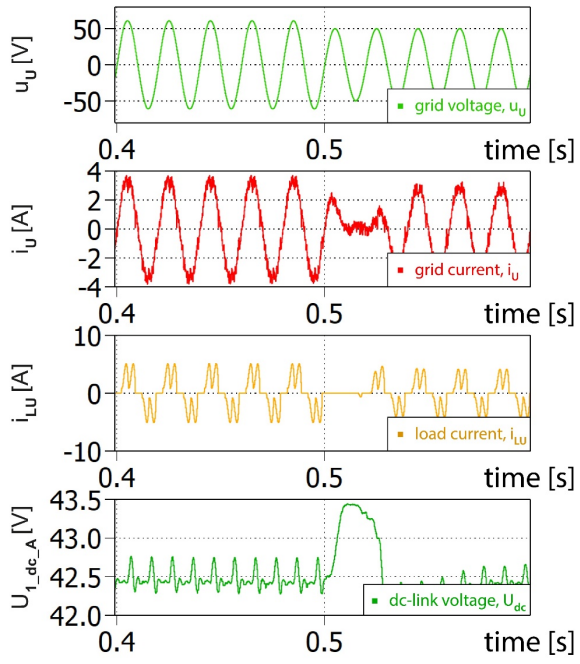

Figure 13. APF with two-step FCS-MPC control under 10% voltage sag of all the phase voltages in t = 0.5 s. The power grid is loaded by the 3ph diode rectifier supplying an RC load with R = 32 Ω,C = 3.25 mF. U_{dc_ref} = 42.5 V (*U_{dc_tot} = 170 V). APF, active power filter; FCS-MPC, finite control set model predictive control; RC,

The proposed two-step FCS-MPC control was also verified under voltage sag in the power grid (see Figure 13). The transient occurs in a simulation time of 0.5 s, and it was caused by a 10% voltage drop in all phases. This transient state had no other effects on the compensation of the power grid.

5. Experimental Results

A detailed experimental study on the 60 kW APF prototype was performed to verify the possibility of implementing the control to a conventional digital signal microcontroller (DSP) and to verify the proposed APF configuration in real-time operational conditions. The hardware of the APF prototype is based on a universal H-bridge converter for cascaded multilevel topologies (SHRack) (Kehl et al., 2021). The SHRack converter consists of four H-bridge modules housed in a 2U height 19″ rack enclosure. The rated power of the SHRack converter is 20 kW (5 kW per H-bridge). The rated voltage of individual H-bridge converters is 750 Vdc. SHRack is designed for an operating voltage of 1 kVdc, so in the case of four CHB cells, the operating voltage is 250 V DC per H-bridge. The rated current of the H-bridge cell is 36 Arms. The H-bridged driver modules are designed for operation with switching frequency up to 16 kHz. Each H-bridge cell of the SHRack converter is equipped with the measurement of the DC-link voltage, the temperature of the IGBT module, and output current. Figure 19 displays the developed testbed photo.

The TMS320F28377 controller was used for the implementation of control. The selected TI 28377 is the gold standard for industry applications at present. The recent industry demands for APF designs require the switching frequency over 10 kHz for several reasons (NVH – noise, vibration and harshness, current ripple, passives, etc.). Therefore, the minimum sampling frequency was set to 10 kHz, corresponding to 100 μs of the sampling time. The implementation of the full-state FCS-MPC, which was selected as a reference control, even with the support of existing computation optimizations took over 140 μs in target TMS320F28377 (i.e. it disqualifies this technology for the industry applications at present). The market analysis was performed to find an alternative to TI TMS320F28377, i.e. a microcontroller or signal processor with comparable cost but significantly higher computation power. The platforms, such as NXP Kineis KV5x (32-bit Cortex-M7, 240 MHz), Infineon XMC7100 (32-bit Cortex-M7, 250 MHz),

or STMicroelectronics STM32G4xx (32-bit Cortex-M4, 170 MHz), were considered. However, these alternatives have not only comparable cost but also comparable computation power. We did not find an industry-recognized alternative allowing the implementation of conventional full-state FCS-MPC with a sampling frequency of 100 µs. Hence, this paper can only provide the experiments performed on the developed APF prototype for novel control. The detailed controller hardware analysis discovered another constraint of the investigated MPC—it is the limited scalability when the processor without supporting FPGA is used. If the number of cascaded CHB cells increases, the computation complexity and necessary computation power increase too. For five cascaded cells (11-level output voltage), the calculation of the proposed two-step FCS-MPC on TMS320F28377 took 113 µs and exceeded the defined limit of 100 µs. Hence, it can be concluded that the implementation limit for the proposed control using a similarly powerful processor and demanded sampling period below 100 µs is 9L CHB converter. For higher numbers of cascaded cells in the CHB converters, it would be necessary to use FPGA or multi-core processors allowing parallel calculations.

The APF prototype was tested under steady-state and selected transient conditions. First, the APF start-up was investigated (Figure 14). Figure 14a analyses the APF start-up transient. At the end of the initial pre-charging procedure, all DC-links of each CHB converter of the APF are charged to grid maximum voltages, and the grid current corresponds to the load current. The load is represented by the three-phase diode bridge rectifier with the RC load, as mentioned above. After starting the APF control, the DC-link voltage of particular CHB cells rises to the demanded DC-link voltage (U_{dc_ref} = 42.5 V for each H-bridge, *U_{dc_tot} = 170 V), and the grid current started to be near sinewave. Figure 14b shows steady-state operation after APF start-up in the same experimental setup. In the next tests, the APF behaviour under the power grid load changes was explored. Figures 15 and 16 report the experiments with the step changes of the power grid load. In the interval I in Figure 15, the grid load is given by the 3ph diode bridge rectifier with an RC load with R = 32 Ω,C = 3.25 mF. At the beginning of interval II in Figure 15, the grid is unloaded (the resistor in the rectifier DC-link is disconnected), which results in a slight overshoot of DC-link voltages. The grid is loaded again with the same load as in interval I at the beginning of interval III in Figure 15, which leads to a minor drop in DC-link voltages. The proposed control responds with appropriate dynamics to these phenomena.

Big attention was paid to the balancing of DC-link voltages in CHB converters and their cells under different operating conditions—including the fault condition operation (the fault condition was e.g. emulated by additional load introduced by resistors connected in parallel to DC-link capacitors of one or more CHB cells). Figure 17 demonstrates the ability of the proposed control with improved PQ theory, wherein three total DC-link voltage PI controllers are implemented instead of a single PI controller of U_{dc_tot}. Figure 17a illustrates that the single total DC-link voltage PI controller is insufficient to balance the voltages among all the DC-links of the CHB converters regardless of whether the conventional full-state or proposed two-step FCS-MPC approach is employed. U_{dc_ref} was set to 42.5 V. However, in the experiment with the single total DC-link PI controller, the voltage levels for one CHB converter were only around 39 V and more distorted. In the case of the proposed three PI controllers, DC-links of all CHB converters were properly balanced. Figure 18 shows the balancing performance of the same control

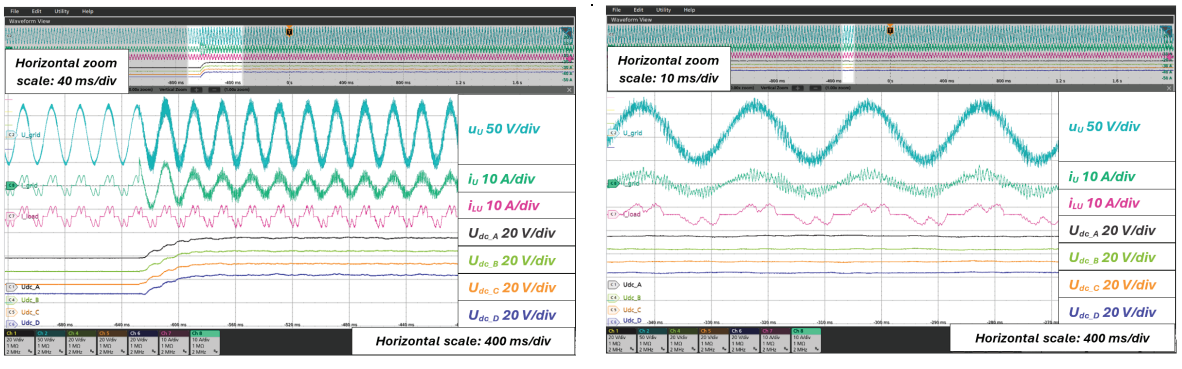

Figure 14. APF start-up under two-step FCS-MPC control: (a) start-up transient and (b) steady-state after the start-up. Power grid loaded by the 3ph diode rectifier supplying RC load with R = 32 Ω, C = 3.25 mF. U_{dc_ref} = 42.5 V (*U_{dc_tot} = 170 V). Cyan: grid voltage [50V/div], green: grid (compensated) current [10A/div], purple: load current [10A/div], DC-link voltages in one CHB converter [20V/div]. APF, active power filter; CHB, cascaded H-bridge; FCS-MPC, finite control set model predictive control; RC,

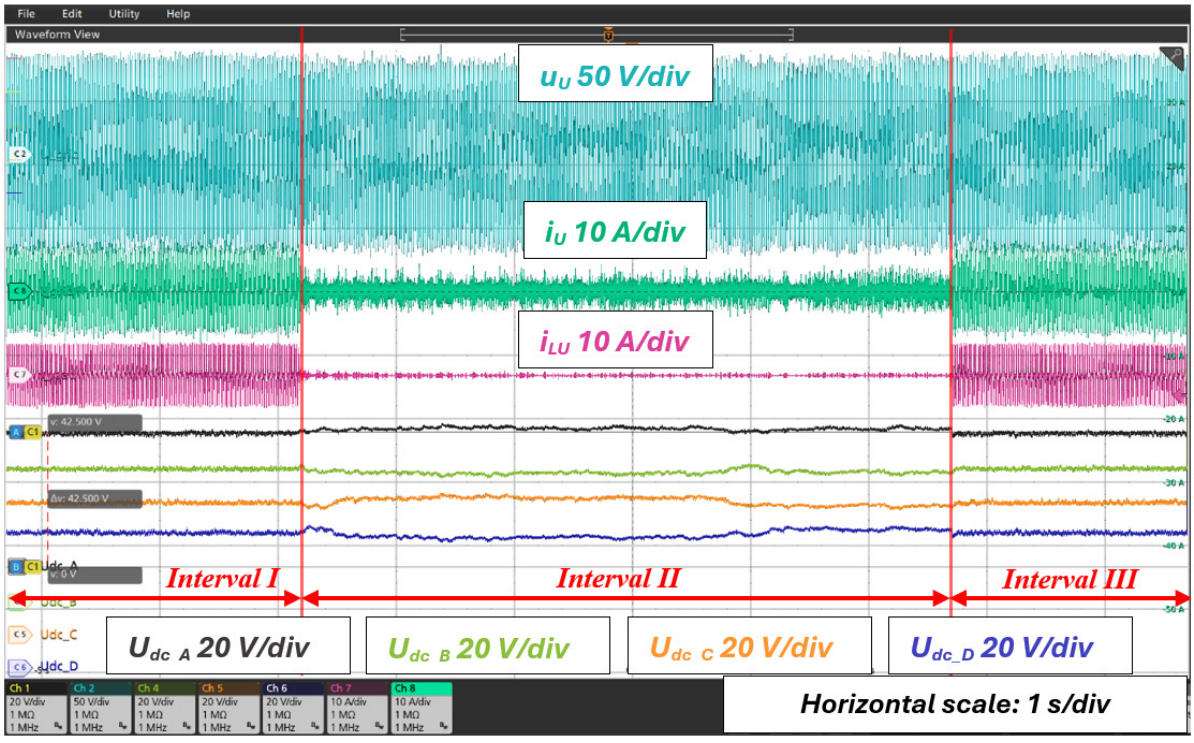

Figure 15. Response of APF with two-step FCS-MPC to step changes in the power grid load. Interval I and III—power grid loaded by 3ph diode rectifier supplying RC load with R = 32 Ω, C = 3.25 mF. Interval II—unloaded grid. U_{dc_ref} = 42.5 V ($^{*}U_{dc\_tot}$ = 170 V). Cyan: grid voltage [50V/div], green: grid (compensated) current [10A/div], purple: load current [10A/div], DC-link voltages in one CHB converter [20V/div]. APF, active power filter; CHB, cascaded H-bridge; FCS-MPC, finite control set model predictive control; RC,

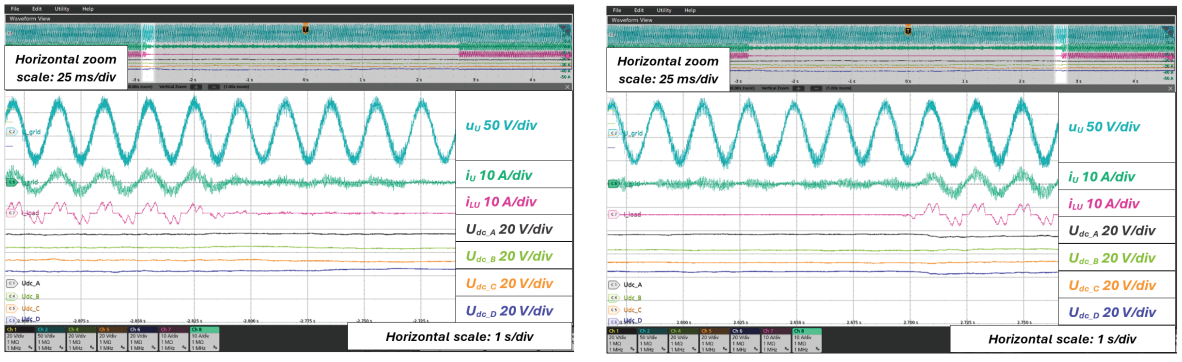

Figure 16. Response of APF with two-step FCS-MPC to step changes in the power grid load—detail of Figure 16: (a) unloading of the power grid (transition interval I II) and (b) step loading of the grid (transition interval II III). Cyan: grid voltage [50V/div], green: grid (compensated) current [10A/div], purple: load current [10A/div], DC-link voltages in one CHB converter of the active filter [20V/div]. APF, active power filter; CHB, cascaded H-bridge; FCS-MPC, finite control set model predictive control.

configuration during a fault in one CHB converter in phase 1. The CHB converter DC-link *B* in phase 1 of the APF was loaded with a parallel resistance of R = 85 Ω, which caused unsymmetrical operational condition in this CHB converter.

To quantify the proposed algorithm performance, the THD of the (compensated) grid current was calculated using a simulation model for the conventional full-state FCS-MPC and the proposed two-step FCS-MPC, respectively. Consequently, the THD of the measured compensated grid current in experiments was also calculated. The results are summarized in Table 1.

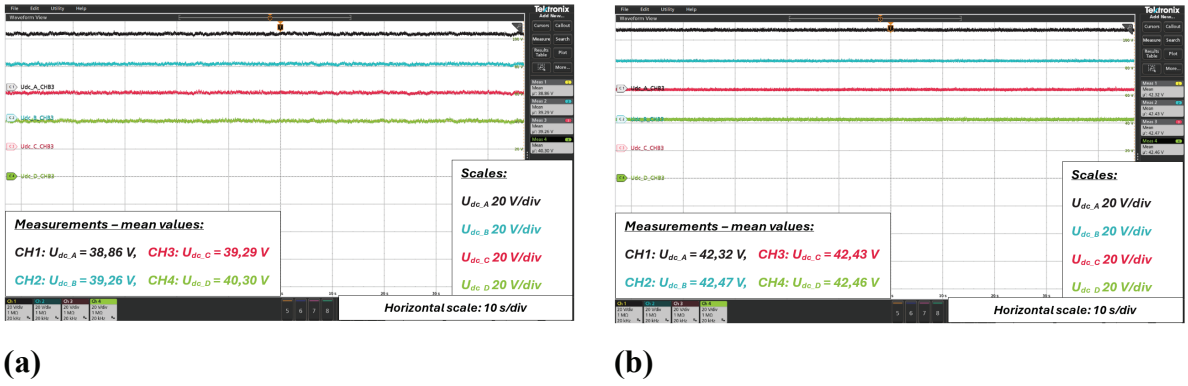

Figure 17. Balancing of DC-links of CHB converters—steady-state: (a) two-step FCS-MPC with one U_{dc_tot} voltage controller in power grid control (control level 1), (b) two-step FCS-MPC with three separated U_{dc_tot} in the power grid control. U_{dc_ref} = 42.5 V (*U_{dc_tot} = 170 V). All channels: [20V/div]. CHB, cascaded H-bridge; FCS-MPC, finite control set model predictive control.

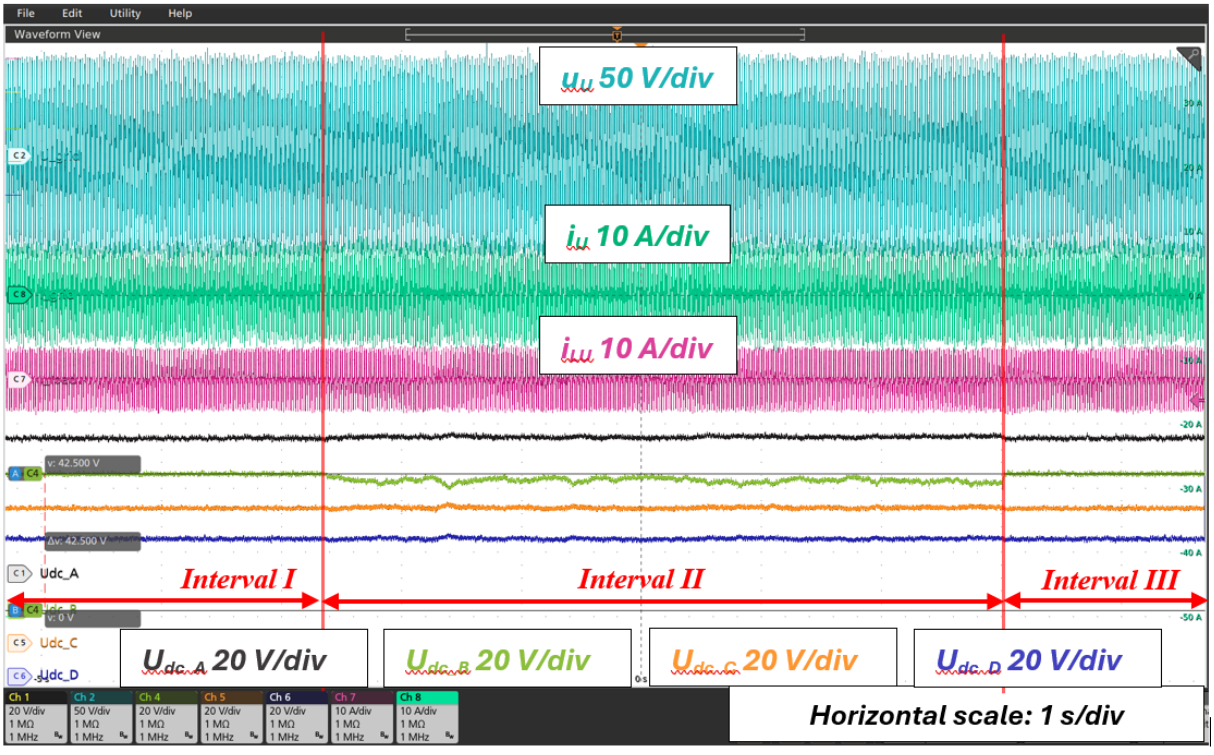

Figure 18. Balancing of DC-links of CHB converters—fault in DC-link in cell B of CHB converter 1 caused by parallel resistance R = 85 Ω to C_{dc} in interval II. Interval I and III without fault. U_{dc_ref} = 42.5 V (*U_{dc_tot} = 170 V). All channels: [20V/div]. CHB, cascaded H-bridge.

The experimental and simulation results demonstrate the investigated APF configuration's effectiveness and the proposed control's benefits. The control successfully manages start-up, steady-state operation, and dynamic load changes while maintaining stable DC-link voltages and effectively filtering grid currents. The proposed two-step FCS-MPC significantly reduces computation time while keeping the control quality comparable to full-state FCS-MPC. The improved power grid control while incorporating three separate PI controllers for DC-link voltage balancing outperforms the conventional single-controller approach, enabling better voltage balancing across each CHB converter of the APF and in individual cells of CHB converters. These findings confirm the robust performance of the APF under various operational conditions, including demanding transient load changes. The feasibility of implementing the control in the conventional 'low-cost' microcontroller was also validated.

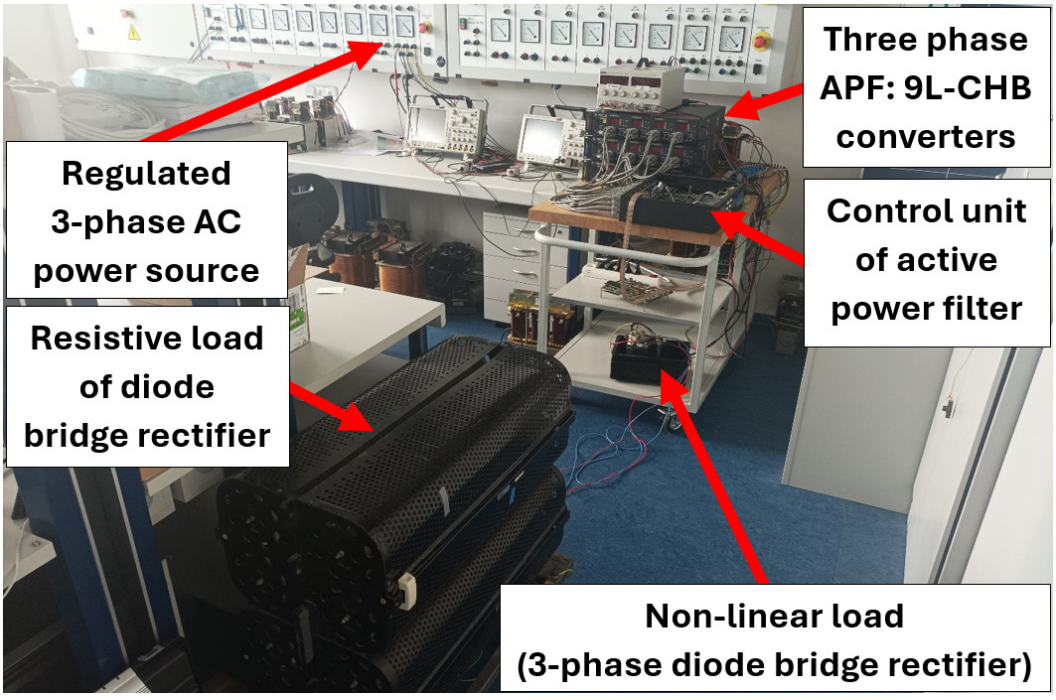

Figure 19. Designed laboratory prototype of three-phase APF 60 kW. APF, active power filter; CHB, cascaded H-bridge.

6. Conclusion

This paper introduced the novel control strategy for shunt-type APFs based on a delta-connected CHB topology. The control is split into two main tasks that can be interpreted as the two levels of APF's control: (1) power grid control and subordinate (2) control of CHB converters forming the APF hardware. The power grid control (control level 1) uses modified instantaneous active-reactive power (PQ) theory, achieving better voltage balancing across each CHB converter of the APF and in individual cells of CHB converters. The control of CHB converters (control level 2) employs the optimized two-step FCS-MPC strategy. This control significantly reduces the computation time and complexity while keeping the control performance comparable to full-state FCS-MPC. Thus, the key contribution of the control is that it can be easily implemented in 'low-cost' microcontrollers without requiring FPGA parallel computation.

The performance of the proposed two-step FCS-MPC was systematically compared with the conventional full-state FCS-MPC in simulations. Both methods achieved similar results regarding the THD of the compensated grid currents, with values of 9.0% for the full-state FCS-MPC and 9.2% for the two-step method. During experimental testing on the 3ph 60 kW APF prototype, the proposed control achieved a THD of 9.9983%. However, a direct comparison with the full-state FCS-MPC in experiments was not possible, as the computational demands of the full-state approach exceeded the capabilities of the TMS320F28377 microcontroller operating with a sampling period of 100 µs. In contrast, two-step FCS-MPC required at most 51 µs to execute (i.e. the computation time has been reduced on the same control hardware below 33% of the conventional full-state FCS-MPC).

The extensive simulation and experimental validation performed on the developed APF prototype of 60 kW confirmed that the proposed control effectively compensates grid harmonics and reactive power, operates reliably under grid and load dynamic changes, and can be implemented in conventional, cost-effective digital controllers.

Acknowledgments

This research has been supported by Ministry of Education, Youth and Sports of the Czech Republic under the project OP JAK Czech Incubator of Technologies for Energy Networks.

References

Abu-Rub, H., Holtz, J., Rodriguez, J. and Baoming, G. (2010). Medium-Voltage Multilevel Converters—State of the Art, Challenges, and Requirements in Industrial Applications. *IEEE Transactions on Industrial Electronics*, 57(8), pp. 2581–2596. doi: 10.1109/TIE.2010.2043039

Akagi, H., Aredes, M. and Watanabe, E. H. (2007). *Instantaneous Power Theory and Applications to Power Conditioning*. John Wiley & Sons, Inc., Hoboken, New Jersey. doi: 10.1002/0470118938

Al-Gahtani, S. F., Salem, E. Z. M., Irshad, S. M. and Azazi, H. Z. (2022). Improved Instantaneous Reactive Power (PQ) Theory Based Control of DVR for Compensating Extreme Sag and Swell. *IEEE Access*, 10, pp. 75186–75204. doi: 10.1109/ACCESS.2022.3185662

Babu, N. P., Guerrero, J. M., Siano, P., Peesapati, R. and Panda, G. (2021). An Improved Adaptive Control Strategy in Grid-Tied PV System with Active Power Filter for Power Quality Enhancement. *IEEE Systems Journal*, 15(2), pp. 2859–2870. doi: 10.1109/JSYST.2020.2985164

Behrouzian, E. (2017). *On Control of Cascaded H-Bridge Converters for STATCOM Applications*. Dissertation. Chalmers University of Technology, Gothenburg, Sweden.

Benhamadouche, A. D., Sahli, A., Bakhi, H., Ballouti, A. and Drif, M. (2023). Enhanced FPGA-Based Controller for Three Phase Shunt Active Power Filter. *Power Electronics and Drives*, 8(43), pp. 128–141. doi: 10.2478/pead-2023-0010

Blahnik, V., Kosan, T., Peroutka, Z. and Talla, J. (2018). Control of a Single-Phase Cascaded H-Bridge Active Rectifier Under Unbalanced Load. *IEEE Transactions on Power Electronics*, 33(6), pp. 5519–5527. doi: 10.1109/TPEL.2017.2748218

Chauhan, A. and Thakur, R. (2016). Power Quality Improvement using Passive & Active Filters. *International Journal of Engineering Trends and Technology (IJETT)*, 36(3), pp. 130–136. doi: 10.14445/22315381/IJETT-V36P225

Ferreira, S. C., Gonzatti, R. B., Pereira, R. R., da Silva, C. H., da Silva, L. E. B. and Lambert-Torres, G. (2018). Finite Control Set Model Predictive Control for Dynamic Reactive Power Compensation with Hybrid Active Power Filters. *IEEE Transactions on Industrial Electronics*, 65(3), pp. 2608–2617. doi: 10.1109/TIE.2017.2740819

Gadalla, A. S., Hasabelrasul, H., Altahir, S. Y. and Yan, X. (2017). Evaluating the Capacity of Power and Energy Balance for Cascaded H-Bridge Multilevel Inverter Using Different PWM Techniques. *The Journal of Engineering*, 2017(13), pp. 1713–1718. doi: 10.1049/joe.2017.0624

He, T., Lu, D. D.-C., Aguilera, R. P., Wu, M., Liu, Q. and Vazquez, S. (2023). Low Computational Burden Model Predictive Control for Single-Phase Cascaded H-Bridge Converters without Weighting Factor. *IEEE Transactions on Industrial Electronics*, 70(3), pp. 2396–2406. doi: 10.1109/tie.2022.3167133

Hrbac, R., Mlcak, T. and Kolar, V. (2017). Improving Power Quality with the Use of a New Method of Serial Active Power Filter (SAPF) Control. *Elektronika ir Elektrotechnika*, pp. 15-20. 23(1). doi: 10.5755/j01.eie.23.1.17578

Karamanakos, P., Pavlou, K. and Manias, S. (2014). An Enumeration-Based Model Predictive Control Strategy for the Cascaded H-Bridge Multilevel Rectifier. *IEEE Transactions on Industrial Electronics*, 61(7), pp. 3480–3489. doi: 10.1109/tie.2013.2278965

Kehl, Z., Glasberger, T. and Streit, L. (2021). Design of universal H-bridge converter for cascaded multilevel topologies. In: *2021 International Conference on Applied Electronics (AE*), Pilsen, Czech Republic, 2021, pp. 1–4. doi: 10.23919/AE51540.2021.9542896.

Leon, J. I., Vazquez, S. and Franquelo, L. G. (2017). Multilevel Converters: Control and Modulation Techniques for Their Operation and Industrial Applications. *Proceedings of the IEEE*, 105(11), pp. 2066–2081. doi: 10.1109/JPROC.2017.2726583

Liang, X. (2016). Emerging power quality challenges due to integration of renewable energy sources. In: *IEEE Industry Applications Society Annual Meeting*, Portland, OR, USA, 2016, pp. 1–9. doi: 10.1109/IAS.2016.7731973.

Limongi, L. R., da Silva, Filho, L. R., Genu, L. G. B., Bradaschia, F. and Cavalcanti, M. C. (2015). Transformerless Hybrid Power Filter Based on a Six-Switch Two-Leg Inverter for Improved Harmonic Compensation Performance. *IEEE Transactions on Industrial Electronics*, 62(1), pp. 40–51. doi: 10.1109/TIE.2014.2327571

Milanović, J. V. (2013). Economic impact of power quality disturbances on customers and utilities. In: *IET Conference on Power in Unity: A Whole System Approach*, London, 2013, pp. 1–37. doi: 10.1049/ic.2013.0158.

Morales-Caporal, R., Bonilla-Huerta, E., Ordoñez-Flores, R. A., Valdez-Fernández, A. and Rangel-Magdaleno, J. D. J. (2024). Finite-Control-Set Model Predictive Control for Single-Phase CHB 5-Level Inverter as an Active Power Filter With Discrete-Time FO-PI DC-Link Controller. *IEEE Access*, 12, pp. 57478–57491. doi: 10.1109/access.2024.3391796

Pereda, J. and Dixon, J. (2012). 23-Level Inverter for Electric Vehicles Using a Single Battery Pack and Series Active Filters. *IEEE Transactions on Vehicular Technology*, 61(3), pp. 1043–1051. doi: 10.1109/TVT.2012.2186599

Po, L., Jingrui, Z., Ruiyu, L., Zheng, F. and Tianying, S. (2018). Composite Adaptive Model Predictive Control for DC-DC Boost Converters. *IET Power Electronics*, 11(10), pp. 1706–1717. doi: 10.1049/iet-pel.2017.0835

Sanjan, P., Gowtham, N., Bhaskar, M., Subramaniam, U., Almakhles, D., Padmanaban, S. and Yamini, N. (2020). Enhancement of Power Quality in Domestic Loads Using Harmonic Filters. *IEEE Access*, 8, pp. 197730–197744. doi: 10.1109/ACCESS.2020.3034734

Satpathy, G. and De, D. (2024). A Novel Proportional Multi-Resonant Current Controller Strategy for Reduced DC Voltage fed D-STATCOM with Internal LCL Resonance Damping. *Power Electronics and Drives*, 9(44), pp. 122–141. doi: 10.2478/pead-2024-0008

Su, W., Lin, C. and Huang, C. (1998). Hybrid Filter Application for Power Quality Improvement. *Electric Power Systems Research*, 47, pp. 165–171. doi: 10.1016/S0378-7796(98)00046-7

Tadayon, M., Hooshmand, R.-A., Kiyoumarsi, A. and Esfahani, M. T. (2021). Imposing Fair Penalty to the Harmonic Sources Based on the Measurement Data. *IET Gener. Transm. Distrib*, 15, pp. 2446–2459. doi: 10.1049/gtd2.12189

Tareen, W. U. K. and Mekhielf, S. (2018). Three-Phase Transformerless Shunt Active Power Filter with Reduced Switch Count for Harmonic Compensation in Grid-Connected Applications. *IEEE Transactions on Power Electronics*, 33(2018), pp. 4868–4881. doi: 10.1109/TPEL.2017.2728602

Teodorescu, R., Loh, P. C., Blaabjerg, F. and Liserre, M. (2006). Proportional-Resonant Controllers and Filters for Grid-Connected Voltage-Source Converters. *IEE Proceedings – Electric Power Applications*, 153(5), p. 750. doi: 10.1049/ip-epa:20060008

Ullah, I. and Ashraf, M. (2019). Sliding Mode Control for Performance Improvement of Shunt Active Power Filter. *SN Appl. Sci*, 1, p. 531. doi: 10.1007/s42452-019-0554-9

Wodyk, S. and Iwanski, G. (2024). Decoupled Control of an Active Power Filter in a Vibrating Reference Frame. *Power Electronics and Drives*, 9(1), pp. 502–518. doi: 10.2478/pead-2024-0031

Xiao, Q., Jia, H., Tang, Y., Jin, Y., Mu, Y., Teodorescu, R. and Blaabjerg, F. (2023). Dual-Layer Modulated Model Predictive Control Scheme for the Cascaded H-Bridge Converter. *IEEE Transactions on Industrial Electronics*, 70(10), pp. 9751–9763. doi: 10.1109/tie.2022.3224185

Zhou, L. and Preindl, M. (2022). Optimal Tracking and Resonance Damping Design of Cascaded Modular Model Predictive Control for a Common-Mode Stabilized Grid-Tied LCL Inverter. *IEEE Transactions on Power Electronics*, 37(8), pp. 9226–9240. doi: 10.1109/tpel.2022.3159599

Appendix I – switching combinations of 9L_CHB converter

Index of switching combination	Group	Output voltage u_{l_CHB}	X_{l_A}	X_{l_B}	X_{l_C}	X_{l_D}
0	0	Udc	1	1	1	1
1	1	3/4 Udc	1	1	1	0
2		3/4 Udc	1	1	0	1
3		3/4 Udc	1	0	1	1
4		3/4 Udc	0	1	1	1
5	2	1/2 Udc	1	1	1	-1
6		1/2 Udc	1	1	0	0
7		1/2 Udc	1	1	-1	1
8		1/2 Udc	1	0	1	0
9		1/2 Udc	1	0	0	1
10		1/2 Udc	1	-1	1	1
11		1/2 Udc	0	1	1	0
12		1/2 Udc	0	1	0	1
13		1/2 Udc	0	0	1	1
14		1/2 Udc	-1	1	1	1
15	3	1/4 Udc	1	1	0	-1
16		1/4 Udc	1	1	-1	0
17		1/4 Udc	1	0	1	-1
18		1/4 Udc	1	0	0	0
19		1/4 Udc	1	0	-1	1
20		1/4 Udc	1	-1	1	0
21		1/4 Udc	1	-1	0	1
22		1/4 Udc	0	1	1	-1
23		1/4 Udc	0	1	0	0
24		1/4 Udc	0	1	-1	1
25		1/4 Udc	0	0	1	0
26		1/4 Udc	0	0	0	1
27		1/4 Udc	0	-1	1	1
28	3	1/4 Udc	-1	1	1	0
29		1/4 Udc	-1	1	0	1
30		1/4 Udc	-1	0	1	1
31	4	0	1	1	-1	-1
32		0	1	0	0	-1
33		0	1	0	-1	0
34		0	1	-1	1	-1
35		0	1	-1	0	0
36		0	1	-1	-1	1
37		0	0	1	0	-1
38		0	0	1	-1	0
39		0	0	0	1	-1
40		0	0	0	0	0
41		0	0	0	-1	1
42		0	0	-1	1	0
43		0	0	-1	0	1
44		0	-1	1	1	-1
45		0	-1	1	0	0
46		0	-1	1	-1	1
47		0	-1	0	1	0
48		0	-1	0	0	1
49		0	-1	-1	1	1
50	5	-1/4 Udc	1	0	-1	-1
51		-1/4 Udc	1	-1	0	-1
52		-1/4 Udc	1	-1	-1	0
53		-1/4 Udc	0	1	-1	-1
54		-1/4 Udc	0	0	0	-1
55		-1/4 Udc	0	0	-1	0
56	5	-1/4 Udc	0	-1	1	-1
57		-1/4 Udc	0	-1	0	0
58		-1/4 Udc	0	-1	-1	1
59		-1/4 Udc	-1	1	0	-1
60		-1/4 Udc	-1	1	-1	0
61		-1/4 Udc	-1	0	1	-1
62		-1/4 Udc	-1	0	0	0
63		-1/4 Udc	-1	0	-1	1
64		-1/4 Udc	-1	-1	1	0
65		-1/4 Udc	-1	-1	0	1
66	6	-1/2 Udc	1	-1	-1	-1
67		-1/2 Udc	0	0	-1	-1
68		-1/2 Udc	0	-1	0	-1
69		-1/2 Udc	0	-1	-1	0
70		-1/2 Udc	-1	1	-1	-1
71		-1/2 Udc	-1	0	0	-1
72		-1/2 Udc	-1	0	-1	0
73		-1/2 Udc	-1	-1	1	-1
74		-1/2 Udc	-1	-1	0	0
75		-1/2 Udc	-1	-1	-1	1
76	7	-3/4 Udc	0	-1	-1	-1
77		-3/4 Udc	-1	0	-1	-1
78		-3/4 Udc	-1	-1	0	-1
79		-3/4 Udc	-1	-1	-1	0
80	8	- Udc	-1	-1	-1	-1